NUCL SCI TECH (2021) 32:92
https://doi.org/10.1007/s41365-021-00935-6

Experimental study on the penetration characteristics of leaking molten salt in the thermal insulation layer of aluminum silicate fiber

Yun Wang[1,2] · Jian Tian[1,2] · Shan-Wu Wang[1,2] · Chong Zhou[1,2] · Na-Xiu Wang[1,2]

Received: 7 April 2021 / Revised: 5 August 2021 / Accepted: 5 August 2021 / Published online: 3 September 2021

Abstract The molten salt leakage accident is an important issue in the nuclear safety analysis of molten salt reactors. While the molten salt leaks from the pipeline or storage tank, it will contact the insulation layer outside; hence, the processes of penetration and spreading play an important role in the development of leakage accidents. In this study, the penetration and diffusion of leaking molten salt (LMS) in an aluminum silicate fiber (ASF) thermal insulation layer were studied experimentally. A molten salt tank with an adjustable outlet was designed to simulate the leakage of molten salt, and the subsequent behavior in the thermal insulation layer was evaluated by measuring the penetration time and penetration mass of the LMS. The results show that when the molten salt discharges from the outlet and reaches the thermal insulation layer, the LMS will penetrate and seep out from the ASF, and a higher flow rate of LMS requires less penetration time and leaked mass of LMS. As the temperature of the LMS and thickness of the ASF increased, the penetration time became longer and the leaked mass became greater at a lower LMS flow rate; when the LMS flow rate increased, the penetration time and leaked mass decreased rapidly and tended to flatten.

This work was supported by the "Strategic Priority Research Program" of the Chinese Academy of Sciences (No. XDA0201002) and the Youth Innovation Promotion Association of the Chinese Academy of Sciences (No. 2018301).

✉ Jian Tian
tianjian@sinap.ac.cn

1 Shanghai Institute of Applied Physics, Chinese Academy of Sciences, Shanghai 201800, China

2 University of Chinese Academy of Sciences, Beijing 100049, China

Keywords Molten salt reactor · Molten salt leakage · Penetration · Insulation layer

1 Introduction

As one of the generation IV types of nuclear reactors, molten salt reactors (MSRs) are being widely developed and studied around the world to achieve THE promising goals of a higher degree of sustainability, improved safety and reliability, lower costs, and protection from nuclear material proliferation [1–3]. The attractive properties of molten salt coolants, such as their high density and heat capacity, high chemical stability, high boiling point, low viscosity, and low vapor pressure, allow that MSR designs employ forced and passive safety systems working at low system pressure [4–6].

In MSRs, the molten salt serves as both a fission fuel and a coolant, and the characteristics of molten salt with different reactor components have been investigated [7–9]. Molten salt leakage accidents are an important issue in the safety analysis of MSRs [10, 11]. There are many reasons for molten salt leakage accidents, including temperature and quality control problems during the welding process, vessel or pipe stress, failure to perform stress-relief heat treatment after welding, corrosion, and sealing problems on flange connections and valve stems with a rotary fit [12–14]. A molten salt leakage accident may cause heat transfer deterioration, incorrect reactivity insertion, abnormal shutdown of the reactor, leakage of radioactivity, and reaction of molten salt with water and oxygen in the surrounding air, producing toxic gases, all of which seriously affect the safety of MSR equipment and operating personnel [15].

When the molten salt pipeline or storage tank of an MSR leaks, leaking molten salt (LMS) contacts the outer aluminum silicate fiber (ASF) thermal insulation layer, which is commonly used in high-temperature loops [16]. As the molten salt leakage accident continues to develop, and an ideal situation is that the LMS gradually solidifies in the ASF as a result of heat loss to the ambient environment at a lower temperature, a solid cladding consisting of molten salt and ASF can be formed. This cladding may prevent further molten salt leakage, that is, provide self-freezing blocking (SFB) of the molten salt leakage; if SFB really exists, it will be a major advantage of MSR safety.

At present, research on leakage accidents in nuclear reactors is concentrated on many working fluids. Journeau et al. [17] conducted two-dimensional molten core–concrete interaction tests in the VULCANO facility with prototypic oxidic corium and found different ablation behaviors between silica-rich concrete and limestone-rich concrete. Yeon et al. [18]. simulated core melt spreading in a reactor cavity with respect to the FARO and VULCANO experiments using the ANSYS-CFX code and verified the validity of the model. Using computational fluid dynamics (CFD) methodology, Na et al. [19] studied and confirmed the feasibility of adopting a post-flooding strategy for molten corium cooling for APR1400 plants. Ye et al. [20] investigated the flow and heat transfer characteristics of an ex-vessel core melt using a commercial CFD code and found a reasonable trend of corium progression compared with the experimental data from the VULANO VE-U7 test. Jung et al. [21] investigated CO_2 leakage accidents in a sodium fast reactor coupled with an S–CO_2 Brayton cycle and validated their isentropic critical flow model through an experiment of critical flow under supercritical conditions. Jeltsov et al. [22] developed and verified a CFD model simulating the potential transport of steam bubbles to the core to study steam generator leakage in lead-cooled fast reactors.

To date, only a few studies on molten salt leakage accidents have been reported. Based on the ANSYS FLUENT two-dimensional axisymmetric model, Shan et al. [23] simulated the leakage process of a certain nitrate salt leaking to the soil surface and studied the influence of leakage port size, leakage flow rate, and leakage temperature on the leakage process. Wu et al. [24] used a custom-made SYSU-N1 molten nitrate salt to design migration and diffusion experiments of nitrate leaking into quartz sand, and they analyzed the influence of the leakage temperature and leakage height. Using the ANSYS FLUENT two-dimensional axisymmetric model, Zhang et al. [25] simulated the seepage and solidification phenomena of molten nitrate salt in porous media material of quartz sand and compared the simulation results with experimental data.

However, the experimental phenomenon of LMS penetrating through the ASF has rarely been addressed. In MSRs, the molten salt working fluid is commonly fluoride salt, and the working temperature is usually between 550 and 650 °C. When a large amount of high-temperature fluoride salt leaks into the environment, it will spray and splash, seriously threatening the safety of personnel and equipment. In this study, the heat transfer salt (HTS) consisting of KNO_3–$NaNO_2$–$NaNO_3$ (53–40–7 wt%) was chosen as the LMS because of its low melting point, low latent heat, low chemical toxicity, and convenient operation. Experiments on molten salt flowing from a storage tank onto an ASF were designed to simulate the processes of molten salt leakage, penetration, and diffusion, and then qualitative and quantitative investigations, including verifying whether the SFB exists and the influences of LMS temperature and ASF thickness on the process, were conducted.

2 Experimental setup

A test apparatus was constructed to study the penetration and diffusion behaviors of LMS flowing onto ASF at the Shanghai Institute of Applied Physics, Chinese Academy of Sciences. The main equipment of the experimental apparatus includes a molten salt storage tank, electric heaters, a molten salt feeding port, a molten salt leakage port, a molten salt valve, an ASF thermal insulation layer, a molten salt catch tray, a platform scale, a lifter, an argon cylinder, a pressure-reducing valve, thermocouples, a level gauge, a barometer, a handheld camera, a control system, and a data acquisition system. Figure 1 shows a schematic of the designed facility for the experiments with detailed arrangements and notes.

An onsite photograph of the experimental apparatus is shown in Fig. 2. The support frame of the experimental apparatus, a 304 stainless steel structure with four legs and a hole, was used to fix the molten salt storage tank at an appropriate height and provide a platform for experimenters to feed solid salt powder to the molten salt tank. The storage tank was made of 316 L stainless steel with a designed maximum operating temperature of 700.0 °C, and the actual operating temperature was < 650.0 °C. The designed maximum pressure of the molten salt tank was 0.6 MPa, and the actual operating pressure was < 0.3 MPa. The tank can be used to hold nitrate and fluoride salts. The volume of the molten salt tank was $\sim$ 70 L, which can hold $\sim$ 100 kg of molten salt.

Because molten salts tend to absorb water vapor from the air and become very sticky, the diameter of the feeding port should not be too small; otherwise, the sticky salt powder may easily adhere to the inner wall of the feeding

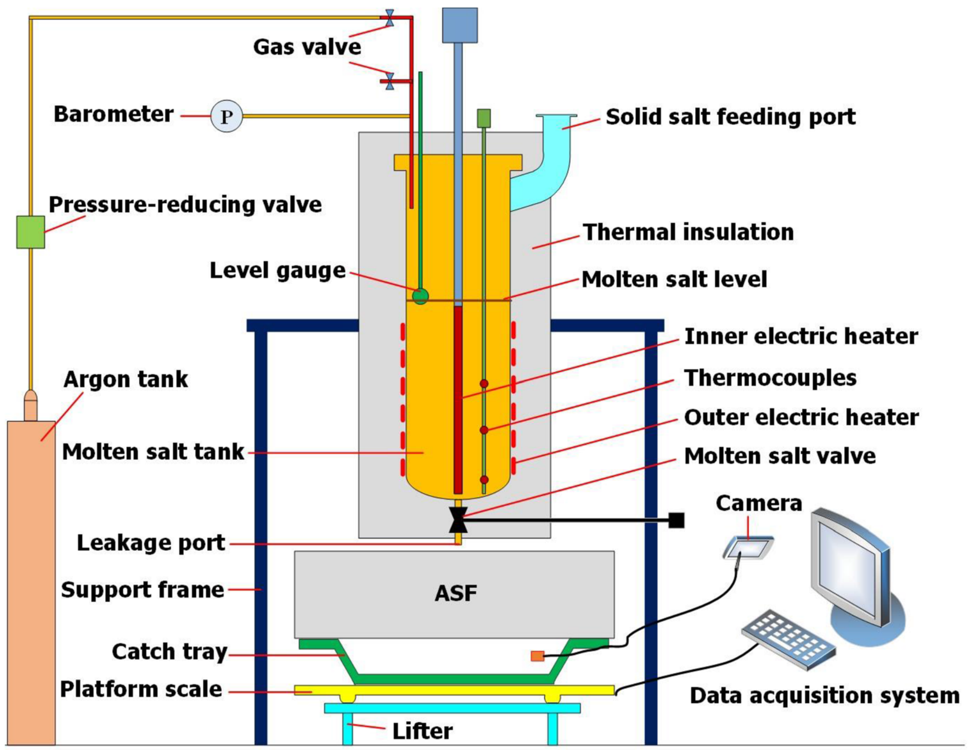

Fig. 1 (Color online) Schematic of the molten salt leakage experimental setup

tube, which could make it difficult to pour the powder further from the feeding port. This greatly reduces the feeding efficiency. A transparent quartz glass window was installed at the feeding port, from which a visual inspection of the molten salt level in the storage tank can be easily obtained.

The external heater of the storage tank was a wall-mounted crawler heater, which was installed in the middle and lower parts of the tank. Approximately 10 kW of thermal power can be gained from the external heater under a 380 V AC power supply. In addition, an inner rod-shaped electric heater with an output power of ~ 3 kW was installed on the axis of the storage tank. The heating section of the inner heater was located in the middle and lower parts. The external heater is the main heat source for salt melting in the storage tank, whereas the inner heater plays an auxiliary role in melting salts. When the solidified block of molten salt in the tank is heated and melted again, owing to the uneven heating from the external heater, the bottom molten salt block melts before the upper molten salt block. Affected by the volume expansion of the liquid molten salt, the storage tank will be subject to a squeezing force from the inside to the outside in the axial and radial directions, which will significantly shorten the service life of the storage tank. With the help of the inner heater, the squeezing force can be greatly reduced because the molten salt can be melted from inside and outside simultaneously.

A molten salt outlet pipe was installed at the bottom of the storage tank. A 316 L stainless steel valve that can operate normally under the design temperature and pressure of the storage tank was installed at the lower part of the outlet pipe to control the flow rate and simulate different leakage conditions. The molten salt leakage port was set at the end of the outlet pipe with an inner diameter of 6.88 mm. A bundle of miniature rod-shaped electric heaters with 1 kW output was installed around the molten salt valve and the outlet pipe to prevent the LMS from freezing and blocking the pipe.

The storage tank and outlet pump were covered by thermal insulation with a thickness of 200 mm to control the outer surface temperature to < 50 °C.

Meanwhile, ASF layers of the same plane dimension and different thicknesses were placed below the molten salt storage tank with the centroid of the ASF layer facing the leakage port. The ASF material used in the experiment was a needled aluminum silicate blanket that complied with the standard GB/T 16,400–2003.

A molten salt catch tray was placed under the ASF layers to collect the LMS oozing from its bottom surface. Three holes with a diameter of 20 mm were set on each side wall to allow the handheld endoscope camera to observe the LMS oozing from the bottom surface of the ASF into the tray.

The molten salt catch tray was placed on an electronic platform scale, which can continuously measure and record

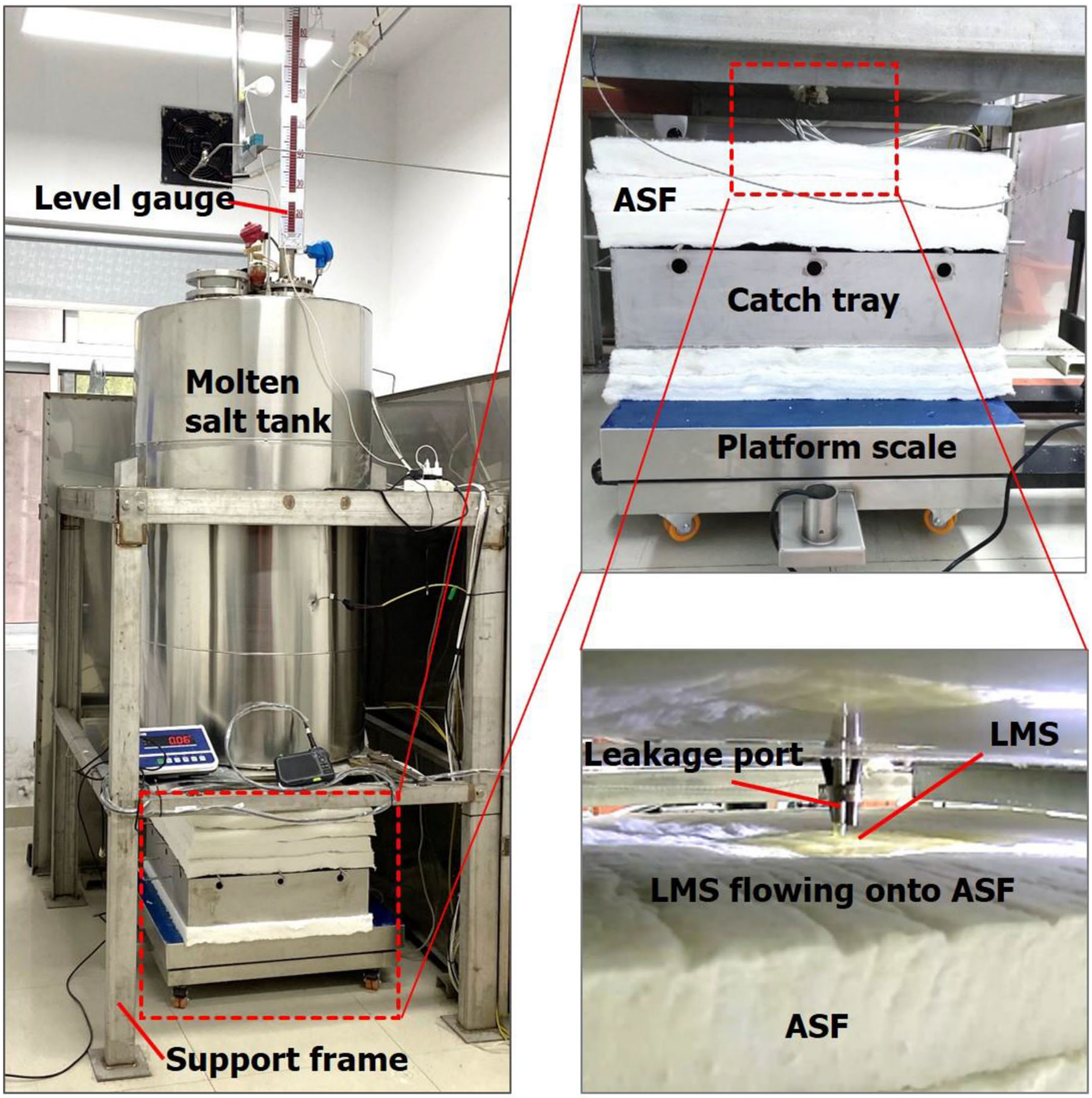

Fig. 2 (Color online) Onsite photograph of the experimental apparatus

mass changes in real time. An insulation layer with a thickness of 100 mm was placed between the molten salt catch tray and platform scale to prevent damage from the high-temperature molten salts.

The electronic platform scale was located on a lifter fork. By lifting the fork, the vertical distance between the molten salt leakage port and the ASF can be freely adjusted. In the present experiment, the distance between the leakage port and the top surface of the ASF was fixed at $\sim$ 10 mm, which is close to the actual molten salt leakage scene of actual pipes or tanks applied in high-temperature loops, and the leakage process can be easily recorded by the surveillance video camera system.

The main design parameters of the experimental apparatus are listed in Table 1.

The control and data acquisition systems include a mass recording system for the platform scale, a control system for the heaters, a recording system for the liquid level gauge, thermocouples, and a video monitoring system.

The leakage rate of the LMS was measured using the electric platform scale. The maximum range of the platform scale was 200 kg, and the measurement accuracy and minimum recording period were 20.0 g and 1.0 s, respectively. The measurement accuracy of the mass change rate can be improved by increasing the recording period of the platform scale.

The molten salt level was measured using a level gauge composed of a floating ball located inside the storage tank and an outside magnetic flap scale. The molten salt level can be visually inspected directly using a magnetic flap

Table 1 Design parameters of the experimental apparatus

Part	Design parameter	
Support frame	Length × width × height (mm^3)	1500 × 1500 × 1600
Molten salt tank	Inner diameter × height (mm^2)	300 × 1000
	Wall thickness (mm)	6.0
	Volume (L)	70
External heater	Electric capacity (kW)	10.0
Inner heating rod	Electric capacity (kW)	3.0
	Length of heating section (mm)	400
Outlet pipe	Length × Outer diameter (mm^2)	Upper part: 150 × 22
		Lower part: 100 × 10
Leakage port	Diameter (mm)	6.88
ASF layer	Length × width (mm^2)	600 × 600
Catch tray	Length × width × height (mm^3)	600 × 600 × 150

scale and recorded automatically by the data acquisition system.

K-type thermocouples with a measuring range of 0–900 °C and an accuracy of 0.5 °C were installed on the tank outer wall, inside the molten salt, and on the inner heater surface to obtain the corresponding temperature data. A high-precision resistance thermometer was used to calibrate these thermocouples before the experiments were started.

The cover pressure of the molten tank was controlled by a gas system comprising an argon cylinder, a pressure-reducing valve, an inlet gas line, an inlet gas switch, an outlet gas line, and an outlet gas switch. The argon cylinder's gas pressure was 14.5 MPa, and the pressure of the storage tank cover gas can be adjusted between 0 and 0.4 MPa. The pressure gauge range of the tank was 0–0.6 MPa with a measurement accuracy of 0.02 MPa.

The measured parameters in the present experiment are listed in Table 2.

The thermal physical properties of the HTS molten salts used in the experiments are listed in Table 3.

3 Experimental method

To quantitatively study the leakage process of LMS in ASF, several important variables were defined for analysis: LMS temperature, LMS flow rate, LMS penetration time, LMS penetration mass, and ASF thickness.

The LMS temperature is the prescribed value to which the molten salt in the storage tank is heated before the leakage experiment starts.

The LMS flow rate was used to simulate the leakage rate and was controlled by adjusting the opening of the molten salt valve and the pressure of the cover gas in the storage tank. It can be obtained through the real-time data of mass change from the platform scale and can be directly used to feedback the adjustment of the molten salt valve during the experiments.

The LMS penetration time was determined by the start and end times of the permeation process. The start time of the LMS is the moment when the first drop of the LMS drips from the leakage port onto the top surface of the ASF, and the end time is the moment when the first drop drips from the bottom surface into the tray. The LMS start and end times can be acquired from the mass change data recorded from the platform scale. During the LMS

Table 2 Measurements and instrument parameters in the experiment

Measurement	Instrument	Parameter	
LMS leakage rate	Platform scale	Maximum range (kg)	200.0
		Minimum recording cycle (s)	1.0
		Accuracy (kg)	0.02
Molten salt level	Level gauge	Maximum range (mm)	1200
		Accuracy (mm)	10.0
Molten salt temperature	Thermocouples (K type)	Range (°C)	0–900
		Accuracy (°C)	0.5
Cover gas pressure	Barometer	Range (MPa)	0–0.4
		Accuracy (MPa)	0.02

Table 3 Properties of HTS molten salt [26]

Parameter	Value
Salt composition	KNO_3–$NaNO_2$–$NaNO_3$ (53–40–7 wt%)
Melting temperature (K)	415.4
Latent heat (kJ/kg)	80
Thermal conductivity (W/(m K))	0.48
Viscosity (kg/(m s))	$0.4737 - 2.297 \times 10^{-3}\,T + 3.731 \times 10^{-6}T^2 - 2.019 \times 10^{-9}T^3$ (420–710 K)
Density (kg/m^3)	$2293.6 - 0.7497\,T$ (470–870 K)
Specific heat (J/(kg K))	1550

penetration time, the total mass of the LMS consumed during penetration is called the penetration mass.

The ASF thickness was determined based on the number of layers of the thermal insulation material. Generally, the thickness of a single layer of ASF was 50 mm, and the thicknesses of 100, 150, and 200 mm corresponded to two, three, and four layers, respectively.

Based on the definitions above, the penetration characteristics of LMS in the ASF can be quantitatively described by the changing tendency of the penetration time and penetration mass with respect to the LMS flow rate, LMS temperature, and ASF thickness. The experimental conditions are presented in Table 4.

3.1 Experiment preparation

Before the start of the experiment, the molten salt valve was completely closed. Approximately 100 kg of solid HTS salt powder was poured into the molten salt storage tank through the feeding port, and the inner and exterior heaters were set at an appropriate heating rate to melt the molten salt gradually to the prescribed temperature. Meanwhile, by continuously filling and expelling the storage tank with argon gas, water vapor and oxygen were gradually removed from the storage tank.

Subsequently, a certain thickness of ASF and the catch tray were placed on the fork of the lifter and then settled directly under the molten salt leakage port. By adjusting the lifter, the vertical distance between the ASF top surface and leakage port was set to ~ 10 mm.

Once the suitable distance between the ASF and leakage port was adjusted by the lifter, the pressure-reducing valve of the gas circuit system was opened to maintain the proper gas pressure in the molten salt storage tank. The pressure can be read from the gas pressure gauge and is in the range of dozens of kilopascals. Therefore, the LMS flow rate could be regulated according to the experimental cases.

Cameras were set at different locations to monitor the experimental situation in real time. Among them, a handheld camera with an endoscope was placed in the catch tray through the side hole and used to closely monitor the conditions of the molten salt leakage at the bottom surface of the ASF. Another camera was set on the top of the ASF, facing the center of the top surface of the ASF, to monitor the situation of molten salt flowing from the leakage port and into the ASF.

By turning on the platform scale's mass recording system and data system, the mass change with respect to time will be recorded and displayed on the screen in real time, and synchronously the corresponding leakage rate can be extracted. Initially, the value of mass tended to be constant, as the rate of mass change went to zero, the process of molten salt leakage was ready to start.

Table 4 Experimental conditions

Parameter	Value
LMS temperature (°C)	200, 300, 400
LMS flow rate (kg/h)	6–500
ASF thickness (mm)	50, 100, 150, 200
Ambience temperature (°C)	19.0–22.0
Pressure of cover gas (kPa)	100

3.2 Molten salt leakage process

Measurement of the molten salt leakage process can be divided into the following steps:

(1) Set the LMS flow rate.
When the molten salt valve is opened, the molten salt flows out of the tank and onto the top surface of the ASF layer. The opening of the molten salt valve was adjusted to control the LMS flow rate in the designed experimental cases. During the entire leakage process, the molten salt valve was adjusted slightly and constantly according to the real-time leakage rate extracted from the platform scale's mass

recording system to maintain the leakage at a constant rate.

(2) Observe the molten salt leakage process.
When LMS flows onto the top surface of the ASF, it is quickly absorbed by the ASF; meanwhile, the LMS continues permeating into the ASF, after which, the LMS reaches the bottom surface of the ASF. As the molten salt penetrates the bottom surface of the ASF, the color of the bottom surface gradually changes from white to light green. As the LMS continues to flow, the bottom surface color gradually deepens and the light green area increasingly expands in the shape of a circle until the molten salt penetrates through the ASF and drops to the bottom of the catch tray. The entire process was recorded in real time by the cameras around the ASF.

(3) Close the molten salt valve.
When the first drop of molten salt dripping from the bottom surface of the ASF is observed from the real-time camera, this indicates that the molten salt has already penetrated through the ASF. The molten salt leakage valve was then closed immediately, and the leakage of the molten salt was stopped. After the molten salt valve is closed, the platform scale's mass data recording is continued until horizontal cumulative mass data with time are displayed on the recording system.

(4) Obtain the molten salt penetration profile.
As soon as the molten salt leakage process is completed, the ASF layers are moved from the molten salt leakage port to the open area by the lifter fork. The diameters of the area where the ASF is immersed in the LMS are then measured. Subsequently, the ASF layer is cut from the center symmetrical line parallel to the side edge of the ASF and divided into two pieces. In this manner, the geometric dimensions of the LMS penetration area inside the ASF can be measured and recorded.

3.3 Data analysis

After the experiment was finished, the mass change data over time of the leakage process were exported to the computer for data post-processing. First, the start and end times of the molten salt leakage process were determined based on the mass measurements from the platform scale. Figure 3 shows the data recorded by the platform scale. The time span from the time at which the mass starts to change to that when it becomes constant again is the molten salt penetration time, and the cumulative mass difference between the start and end times is the molten salt penetration mass. The mass data in the penetration time were chosen for linear fitting, and the slope was the LMS flow rate with respect to the experimental case.

As shown in Fig. 3, the start and end times of the leakage process can be clearly read from the recorded data, and the flow rate from the leakage port to the ASF layer was very stable during the entire leakage process. From the fitting of the data, the LMS flow rate was determined to be 0.034 kg/s (122.4 kg/h). The ASF in this case was penetrated through by LMS, and the penetration mass was 13.6 kg.

4 Experimental results

To investigate the penetration and diffusion trend of LMS in ASF, a series of experiments with an ASF thickness of 50 mm were conducted. For these cases, the LMS temperature was 200 °C and the flow rate was in the range of 6.1–170.3 kg/h. It was found that the ASF is hydrophilic to the molten salt and has a strong ability to absorb LMS. When the LMS constantly flows on the ASF, it diffuses inside the ASF until it penetrates through the ASF. Subsequently, the molten salt continued to ooze from the bottom surface of the ASF and then drop into the catch tray. This indicates that although the ambient temperature is far below the melting point of the HTS molten salt, freezing does not occur at the surface of the ASF, and SFB does not exist. In general, as the flow rate of the LMS increases, the penetration time and mass decrease rapidly at low flow rates and tend to flatten at higher flow rates, as shown in Fig. 4. When the leakage rate of molten salt was 6.1 kg/h, the penetration time was 3540 s and the penetration mass was 6.0 kg. As the flow rate of LMS increased to 74.6 kg/h, the penetration time sharply dropped to 129 s, and the penetration mass decreased to 2.56 kg. With a further increase in the LMS flow rate, the penetration time stabilized, being on the order of tens of seconds, and the penetration mass stabilized between 2 and 3 kg.

When the LMS falls on the top surface of the ASF, owing to the hydrophilicity of ASF, the molten salt permeates vertically and horizontally inside the ASF. In the vertical direction, the permeation is affected by the initial momentum, gravity of the LMS, and absorption of ASF, whereas, in the horizontal direction, the permeation is mainly affected by absorption. The penetration time is a joint effect of the vertical and horizontal permeation of the LMS. When vertical permeation dominates, the penetration time decreases, whereas, when vertical permeation is weak, horizontal permeation will prevail, and the penetration time will increase.

At lower LMS flow rates, because the volume of the LMS falling on the ASF is small, vertical permeation is at a

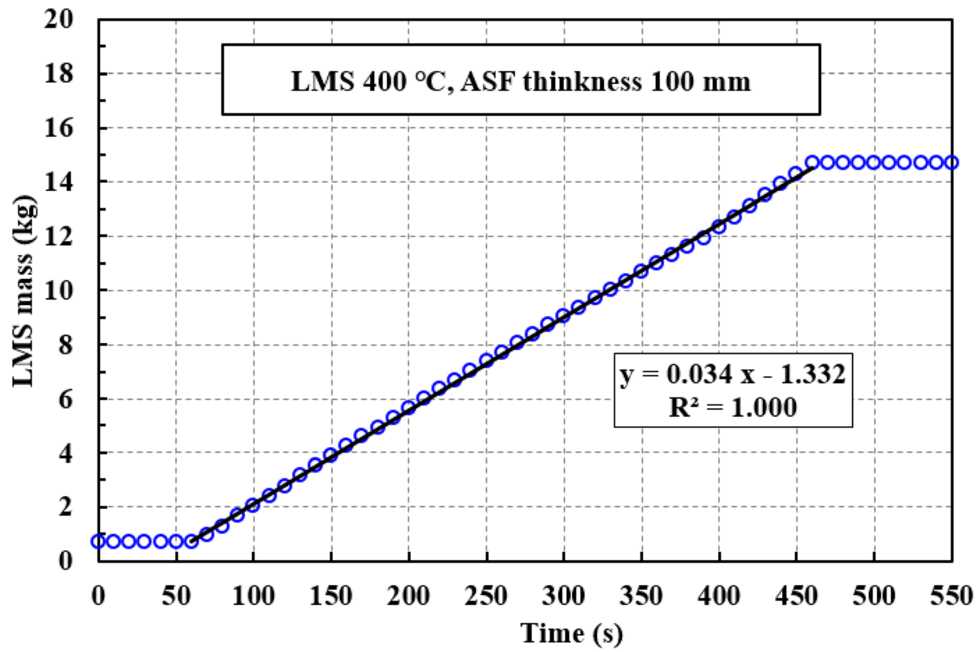

Fig. 3 Leakage mass recorded by the platform scale and data fitting

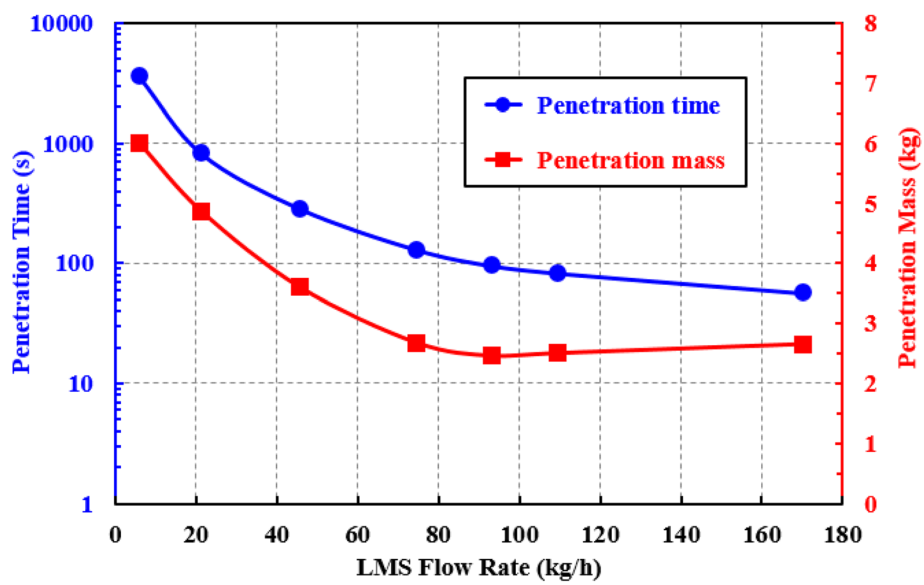

Fig. 4 (Color online) Penetration trend of LMS in ASF

low level; as a result, the LMS has enough time to permeate horizontally before it penetrates through the ASF in the vertical direction; therefore, the penetration time is long. As the LMS flow rate increases, owing to the increasing scale of the LMS, permeation in the vertical direction notably increases, and the penetration time decreases significantly. As the LMS flow rate continues to increase, owing to the large amount of LMS moving in a short time, vertical permeation inside the ASF is completely dominated, and the penetration time mainly depends on the thickness of the ASF.

With respect to the penetration mass, although the LMS flow rate increased, the penetration time dropped more sharply, and, as a result, the penetration mass of LMS corresponding to the leakage rate and penetration time exhibits a decreasing trend.

When the LMS flows onto the ASF, the LMS is quickly absorbed by the ASF owing to its excellent hydrophilic ability for molten salt. Consequently, the ASF is easily penetrated by the LMS. After the LMS penetrates through the ASF, molten salt in the ASF appears in the shape of a circular truncated cone with a smaller diameter on the top surface and a larger diameter on the bottom surface. The zone permeated with high-temperature LMS was light green in color, while the other zones remained the original white color, as shown in Fig. 5.

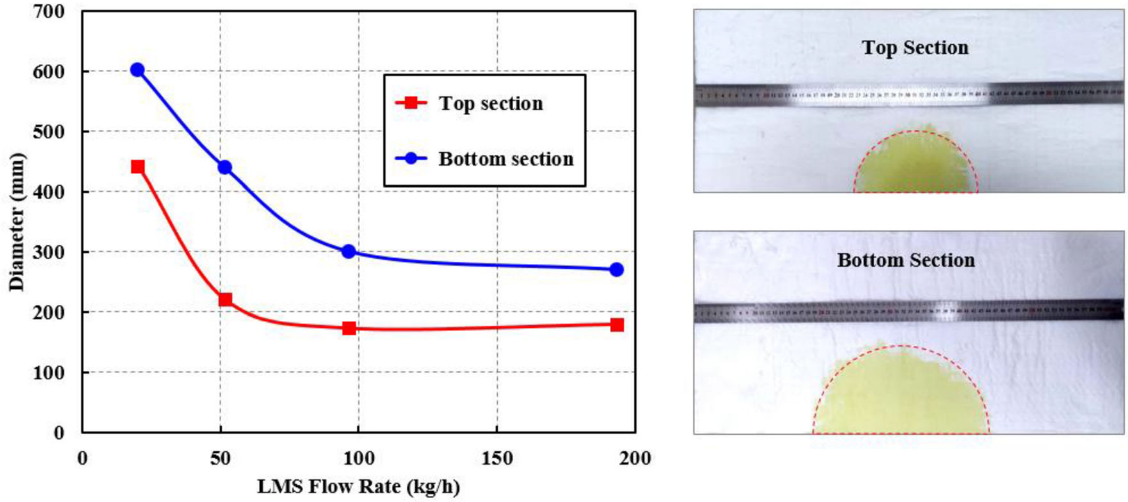

Fig. 5 (Color online) Size of circular truncated cone diameters in ASF under different LMS flow rates

The variation of the circular truncated cone diameters along with different LMS flow rates at an LMS temperature of 300 °C and ASF thickness of 50 mm is illustrated in Fig. 5. It is shown clearly that the contour diameter of the top surface of the cone is always smaller, while the contour diameter of the bottom surface is always larger. As the LMS flow rate increased, both diameters decreased rapidly in the beginning and then tended to flatten; in the end, the difference between the two diameters tended to be invariable. Specifically, when the LMS flow rate was 20.1 kg/h, the diameters of the top and bottom surfaces of the circular truncated cone were 440 and 600 mm, respectively. When the LMS flow rate increased to 193.3 kg/h, the top diameter dropped to 183 mm, while the bottom dropped to 270 mm, as shown in the right panel of Fig. 5. Therefore, the higher the LMS flow rate, the smaller the LMS volume retained in the ASF, and the easier the molten salt penetrates through the ASF.

The behavior of penetration and diffusion for LMS flowing through the ASF was further investigated by inspecting the vertical section of the ASF with different thicknesses (50, 100, 150, and 200 mm) at a comparable LMS flow rate of $\sim$ 20 kg/h, as shown in Fig. 6. It is clear that all the penetration and diffusion trends were similar, and all outlines of the LMS permeation area were approximately the same. For all thicknesses of ASF, molten salt penetrates through the ASF and continues to ooze into the catch tray.

As illustrated above, when the LMS flows onto the ASF, the LMS will permeate inside the ASF vertically and horizontally, owing to the hydrophilicity of the ASF; when the LMS reaches the bottom surface of the ASF, it will not ooze out and drop immediately but will be held by the ASF for a while; as a result, horizontal permeation close to the bottom area will greatly develop, and the vertical section of the LMS in the ASF exhibits the shape of a circular truncated cone, as shown in Fig. 6.

5 Analysis of influencing factors

Through the above experimental research on LMS flowing onto ASF, the penetration and diffusion behaviors are preliminarily known. To further study these behaviors, the effects of LMS temperature and ASF thickness on the penetration time and penetration mass under different experimental conditions were comprehensively investigated.

5.1 Effect of LMS temperature

An ASF thickness of 50 mm was selected to study the influence of the LMS temperature on the penetration behavior. The LMS penetration time and penetration mass as a function of the LMS flow rate with LMS temperatures of 200, 300, and 400 °C are shown in Fig. 7. It is clear that the LMS penetration time and penetration mass generally decrease as the LMS flow rate increases; specifically, the LMS penetration time and penetration mass decrease rapidly at lower LMS flow rates, while they gradually decrease at higher LMS flow rates.

For the cases of lower LMS flow rate, all the LMS penetration times under different temperature cases dropped sharply, and the penetration time tended to be longer as the LMS temperature increased. This indicates that when the temperature of the molten salt is high, it will take a longer time to penetrate through the ASF if the leakage of molten salt is not serious. A possible reason for this is that

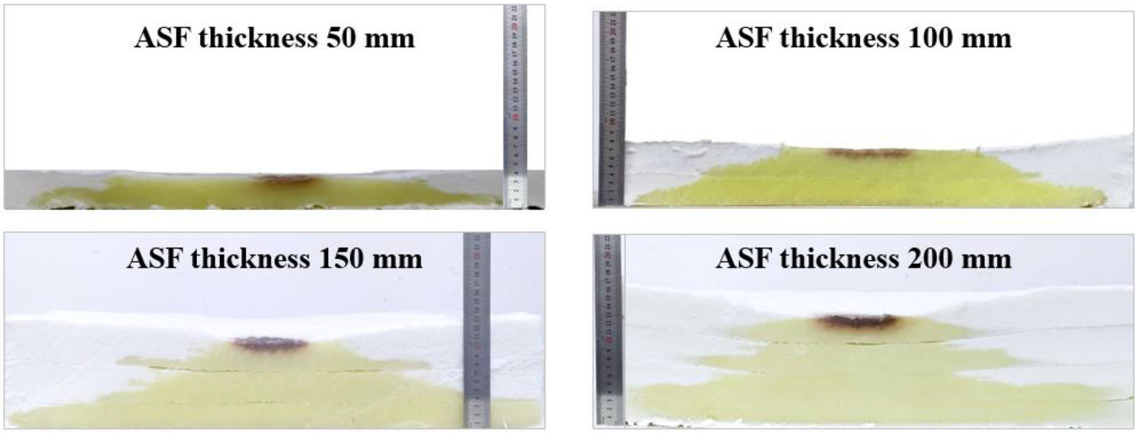

Fig. 6 (Color online) Central section of the molten salt circular truncated cone in the insulation cotton

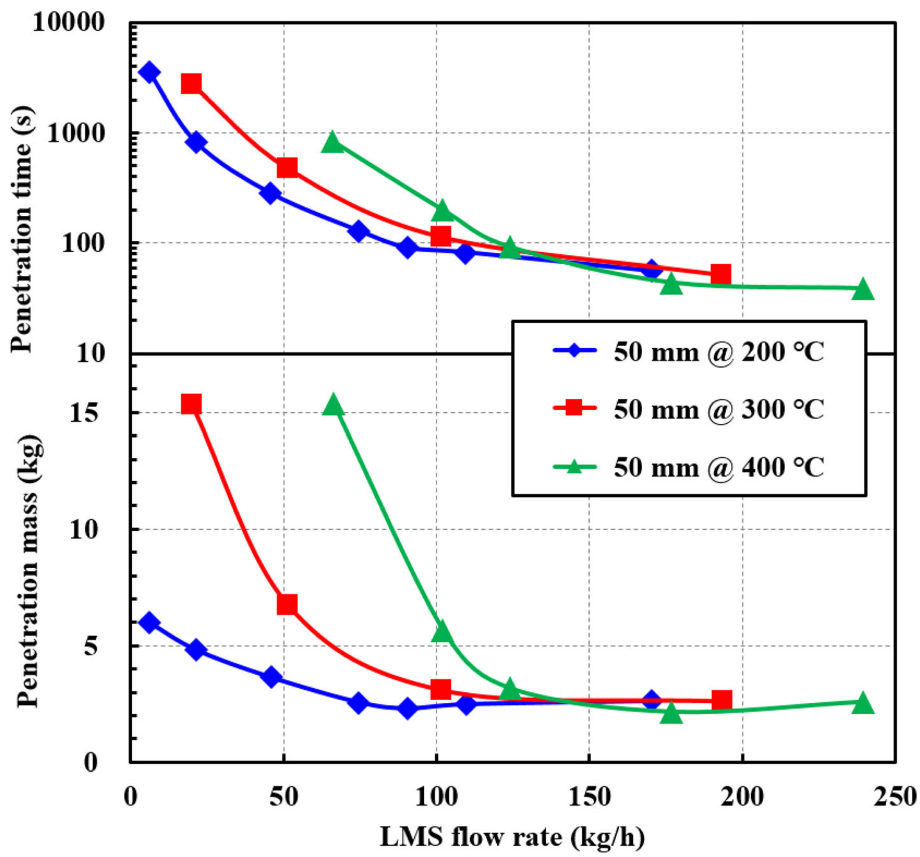

Fig. 7 (Color online) Influence of LMS temperature on penetration time and permeation mass

the higher temperature LMS has a lower viscosity, leading to a greater hydrophilic ability of the ASF. As a result, under a lower LMS leakage rate, the ASF has a longer time to absorb molten salt in the horizontal direction before the LMS penetrates through it. For the cases with a higher LMS flow rate, the LMS penetration time tends to be invariable with the change in LMS temperature and is nearly saturated as the LMS flow rate increases. At a high LMS flow rate, although the hydrophilic ability of the ASF improved at higher LMS temperatures, its absorption ability was almost saturated and could not keep up with the rapidly increasing volume of molten salt leaking from the tank. Consequently, the LMS does not have sufficient time to diffuse into the ASF in the horizontal direction, and the diffusion time in the vertical direction determines the penetration time. In terms of the penetration mass, the same trend with respect to the LMS temperature and flow rate was observed under different experimental cases.

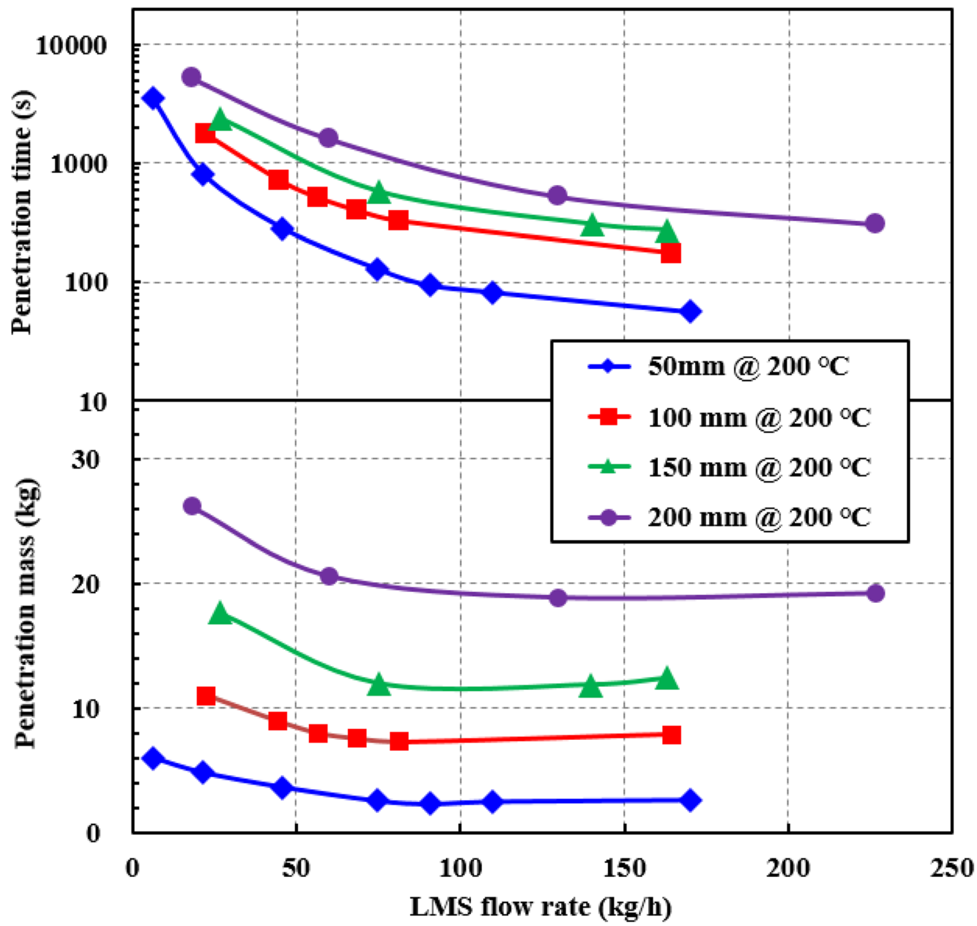

Fig. 8 (Color online) Influence of ASF thickness on penetration time and penetration mass

For the case with an LMS temperature of 200 °C, as the flow rate increased from 6.1 to 110 kg/h, the penetration time dropped sharply from 3540 to 90 s, and, accordingly, the penetration mass dropped from 6 to 2.5 kg, while as the flow rate increased from 110 to 170 kg/h, the penetration time decreased slowly from 90 to 56 s, and, accordingly, the penetration mass increased slightly from 2.5 to 2.6 kg. For the case with an LMS temperature of 300 °C, as the flow rate increased from 20.2 to the 102 kg/h, the penetration time dropped sharply from 2744 to 114 s, and, accordingly, the penetration mass dropped from 15.4 to 3.1 kg, while as the flow rate increased from 102 to 193 kg/h, the penetration time decreased slowly from 114 to 52 s, and, accordingly, the penetration mass dropped from 3.1 to 2.6 kg. For the case with an LMS temperature of 400 °C, as the flow rate increased from 66 to 124 kg/h, the penetration time dropped sharply from 838 to 92 s, and, accordingly, the penetration mass dropped from 15.2 to 3.2 kg, while as the flow rate increased from 124 to 239 kg/h, the penetration time decreased slowly from 92 to 39 s, and, accordingly, the penetration mass dropped from 3.2 to 2.6 kg.

5.2 Effect of ASF thickness

The influence of the ASF thickness on the LMS penetration behavior is shown in Fig. 8. It can be seen that, for all the experimental cases with different ASF thicknesses, the trends of penetration behavior are almost the same: As the LMS flow rate increases, the penetration time decreases and eventually tends to be flat. In the range of lower LMS flow rates, significant differences in penetration time between different experimental cases were observed; specifically, the greater the ASF thickness, the longer the penetration time needed. However, when the flow rate increases to a certain extent, the effect of the ASF thickness on the penetration time notably declines, and the penetration times for different ASF thicknesses gradually tend to be converge. A possible reason for this is that when the leakage rate is low, vertical permeation is relatively slow; consequently, the LMS is easily absorbed and diffused in the horizontal direction. As the thickness increases, the LMS has plenty of time to spread horizontally before it vertically penetrates through the ASF. However, as the LMS flow rate further increases, the LMS penetration along the vertical direction plays a more important role as more molten salt is leaked; therefore, the penetration time is strongly associated with the thickness of the ASF. When the flow rate was ∼ 20 kg/h, the penetration time sharply decreased from 5028 to 816 s as the thickness of the ASF decreased from 200 to 50 mm. When the flow rate was ∼ 170 kg/h, the penetration time slowly decreased from 274 to 56 s as the thickness of the ASF decreased from 150 to 50 mm.

All the cases exhibit a decreasing trend in the penetration mass as the LMS flow rate increases, becoming flat at higher flow rates. For any of flow rates, the penetration mass is almost proportional to thickness of ASF. When the flow rate was ∼ 20 kg/h, the penetration masses were 26.2, 17.7, 11, and 4.9 kg for ASF thicknesses of 200, 150, 100, and 50 mm, respectively, whereas when the flow rate was ∼ 170 kg/h, the penetration masses were 12.4, 7.9, and 2.4 kg for thicknesses of 150, 100, and 50 mm, respectively.

6 Conclusion

In the present study, an experimental apparatus was constructed to investigate the penetration and diffusion of LMS in an ASF thermal insulation layer. Experiments with different LMS flow rates, LMS temperatures, and ASF thicknesses were conducted, and important phenomena were observed.

The ASF exhibits a strong hydrophilic ability to the molten salt, and when the LMS flows onto the ASF, the LMS is quickly absorbed and spreads inside the ASF. For all cases with different thicknesses of ASF, different LMS temperatures, and flow rates, the LMS penetrated and oozed out from the ASF. The phenomenon of SFB was not observed in the current experimental cases.

At low LMS flow rates, the penetration time and penetration mass both exhibit obvious dependencies on the LMS flow rate, LMS temperature, and ASF thickness. Specifically, the lower the LMS flow rate, the higher the LMS temperature, and the thicker the ASF, the longer the penetration time and greater the penetration mass. At higher flow rates, the penetration time and penetration mass tended to be less influenced by the LMS flow rate, LMS temperature, and ASF thickness.

The results from the present work will enhance our understanding of molten salt leakage onto thermal insulation and provide helpful guidance for safety analysis of molten salt leakage accidents.

Author contributions All authors contributed to the study conception and design. Material preparation, data collection, and analysis were performed by Yun Wang and Jian Tian. The first draft of the manuscript was written by Yun Wang, and all authors commented on previous versions of the manuscript. All authors read and approved the final manuscript.

References

1. H.J. Xu, Thorium Energy and Molten Salt Reactor R&D in China, in *Thorium Energy for the World*. ed. by J.P. Revol, M. Bourquin, Y. Kadi et al. (Springer, Cham, 2016), pp. 37–44
2. C.W. Forsberg, P.F. Peterson, P.S. Pickard, Molten-salt-cooled advanced high-temperature reactor for production of hydrogen and electricity. Nucl. Technol. **144**(3), 289–302 (2003). https://doi.org/10.13182/NT03-1
3. B. Mignacca, G. Locatelli, Economics and finance of molten salt reactors. Prog. Nucl. Energy **129**, 103503 (2020). https://doi.org/10.1016/j.pnucene.2020.103503
4. D. F. Williams, L. M. Toth, K. T. Clarno, Assessment of Candidate Molten Salt Coolants for the Advanced High-Temperature Reactor (AHTR), Oak Ridge National Laboratory, ORNL/TM-2006/12
5. C.L. Wang, H. Qin, D.L. Zhang et al., Numerical investigation of natural convection characteristics of a heat pipe-cooled passive residual heat removal system for molten salt reactors. Nucl. Sci. Tech. **31**(7), 65 (2020). https://doi.org/10.1007/s41365-020-00780-z
6. Y.M. Ferng, K.Y. Lin, C.W. Chi, CFD investigating thermal-hydraulic characteristics of FLiNaK salt as a heat exchange fluid. Appl. Therm. Eng. **37**, 235–240 (2012). https://doi.org/10.1016/j.applthermaleng.2011.11.021
7. H.X. Xu, J. Lin, Y.J. Zhong et al., Characterization of molten 2LiF–BeF_2 salt impregnated into graphite matrix of fuel elements for thorium molten salt reactor. Nucl. Sci. Tech. **30**, 74 (2019). https://doi.org/10.1007/s41365-019-0600-8
8. X.Y. Jiang, H.J. Lu, Y.S. Chen et al., Numerical and experimental investigation of a new conceptual fluoride salt freeze valve for thorium based molten salt reactor. Nucl. Sci. Tech. **31**(2), 16 (2020). https://doi.org/10.1007/s41365-020-0729-5
9. Q.M. Li, C. Zhou, J. Tian et al., Avoiding sealing failure of flanged connection for tubes made of dissimilar materials subjected to elevated temperature. Nucl. Sci. Tech. **30**(1), 1 (2019). https://doi.org/10.1007/s41365-018-0540-8
10. C.Y. Li, X.B. Xia, J. Cai et al., Radiation dose distribution of liquid fueled thorium molten salt reactor. Nucl. Sci. Tech. **32**(2), 22 (2021). https://doi.org/10.1007/s41365-021-00857-3
11. C.Q. Chen, X.B. Xia, Z.H. Zhang et al., Radiological environmental impact analysis of a 2-MW thorium molten salt reactor during an accident. Nucl. Sci. Tech. **30**(5), 78 (2019). https://doi.org/10.1007/s41365-019-0605-3
12. L.C. Olson, J.W. Ambrosek, K. Sridharan et al., Materials corrosion in molten LiF–NaF–KF salt. J. Fluor. Chem. **130**, 67–73 (2009). https://doi.org/10.1016/j.jfluchem.2008.05.008
13. X.J. Guo, Z. Ding, G.F. Qin et al., A literature review on some engineering issues of high temperature molten salt thermal energy storage systems. Energy Storage Sci. Technol. **4**(01), 32–43 (2015). https://doi.org/10.3969/j.issn.2095-4239.2015.01.003
14. H. Zhu, R. Holmes, T. Hanley et al., High-temperature corrosion of helium ion-irradiated Ni-based alloy in fluoride molten salt. Corros. Sci. **91**, 1–6 (2015). https://doi.org/10.1016/j.corsci.2014.11.013
15. S. E. Beall, P. N. Haubenreich, R. B. Lindauer et al, MSRE design and operations report, Part V., Reactor safety analysis report. ORNL-TM-732

16. X.Y. Wang, Y.F. Cao, Ceramic fiber as a new material. J. Cellulose Sci. Technol. **20**(1), 79–85 (2012). (in Chinese)
17. C. Journeau, P. Piluso, J. Haquet et al., Two-dimensional interaction of oxidic corium with concretes: the VULCANO VB test series. Ann. Nucl. Energy **36**, 1597–1613 (2009). https://doi.org/10.1016/j.anucene.2009.07.006
18. W. Yeon, K. Bang, Y. Choi et al., CFD analysis of core melt spreading on the reactor cavity floor using ANSYS CFX code. Nucl. Eng. Des. **249**, 90–96 (2012). https://doi.org/10.1016/j.nucengdes.2011.08.047
19. H. Na, H.S. Kim, H.J. Lee et al., Preliminary feasibility study of post-flooding ex-vessel corium cooling strategy by CFD spreading simulations and concrete ablation analysis. Prog. Nucl. Energ. **97**, 139–152 (2017). https://doi.org/10.1016/j.pnucene.2016.12.017
20. I. Ye, J.A. Kim, C. Ryu et al., Numerical investigation of the spreading and heat transfer characteristics of ex-vessel core melt. Nucl. Eng. Technol. **45**, 21–28 (2013). https://doi.org/10.5516/NET.03.2012.011
21. H. Jung, M.S. Kim, A. Ko et al., Investigation of CO_2 leak accident in SFR coupled with S-CO_2 Brayton cycle. Ann. Nucl. Energy **103**, 212–226 (2017). https://doi.org/10.1016/j.anucene.2017.01.013
22. M. Jeltsov, W. Villanueva, P. Kudinov, Steam generator leakage in lead cooled fast reactors: modeling of void transport to the core. Nucl. Eng. Des. **328**, 255–265 (2018). https://doi.org/10.1016/j.nucengdes.2018.01.006
23. J. Shan, J. Ding, J. Lu, Numerical investigation of high-temperature molten salt leakage. Energy Procedia. **69**, 2072–2080 (2015). https://doi.org/10.1016/j.egypro.2015.03.221
24. J.Q. Wu, J. Ding, J.F. Lu et al., Experimental study of the leakage nitrate molten salt in the soil. J. Eng. Thermophys. **38**(6), 1300–1304 (2017). (in Chinese)
25. Y. Zhang, J. Wu, W. Wang et al., Experimental and numerical studies on molten salt migration in porous system with phase change. Int. J. Heat Mass Transf. **129**, 397–405 (2019). https://doi.org/10.1016/j.ijheatmasstransfer.2018.09.122
26. D.R. Wu, *Chemical Process Design Manual*, 4th edn. (Chemical Industry Press, Beijing, 2009). (in Chinese)